



Quantification of cell membrane permeability induced by monopolar and high-frequency bipolar bursts of electrical pulses



Daniel C. Sweeney^a, Matej Reberšek^b, Janja Dermol^b, Lea Rems^{b,1}, Damijan Miklavčič^b, Rafael V. Davalos^{a,*}

^a Virginia Tech, Department of Biomedical Engineering and Mechanics, 330 Kelly Hall, Blacksburg, USA

^b University of Ljubljana, Faculty of Electrical Engineering, Tržaška 25, SI 1000, Ljubljana, Slovenia

ARTICLE INFO

Article history:

Received 20 April 2016

Received in revised form 6 June 2016

Accepted 26 June 2016

Available online 29 June 2016

Keywords:

Electroporation

Bipolar electrical pulses

Permeability

Irreversible electroporation

Gene electrotransfer

Electrochemotherapy

ABSTRACT

High-frequency bipolar electric pulses have been shown to mitigate undesirable muscle contraction during irreversible electroporation (IRE) therapy. Here, we evaluate the potential applicability of such pulses for introducing exogenous molecules into cells, such as in electrochemotherapy (ECT). For this purpose we develop a method for calculating the time course of the effective permeability of an electroporated cell membrane based on real-time imaging of propidium transport into single cells that allows a quantitative comparison between different pulsing schemes. We calculate the effective permeability for several pulsed electric field treatments including trains of 100 μ s monopolar pulses, conventionally used in IRE and ECT, and pulse trains containing bursts or evenly-spaced 1 μ s bipolar pulses. We show that shorter bipolar pulses induce lower effective membrane permeability than longer monopolar pulses with equivalent treatment times. This lower efficiency can be attributed to incomplete membrane charging. Nevertheless, bipolar pulses could be used for increasing the uptake of small molecules into cells more symmetrically, but at the expense of higher applied voltages. These data indicate that high-frequency bipolar bursts of electrical pulses may be designed to electroporate cells as effectively as and more homogeneously than conventional monopolar pulses.

© 2016 Elsevier B.V. All rights reserved.

1. Introduction

Biological membranes are critical to maintaining cellular homeostasis by isolating a cell's interior from its extracellular environment. The cell utilizes its membrane as a barrier to general transport, but allows for the controlled exchange of valuable nutrients, chemical signals, and waste products through transmembrane structures, which shuttle molecules into and out of the cell and maintain the precise homeostatic balance necessary for the cell's function and survival. When biological membranes are exposed to sufficiently intense pulsed electric fields (PEFs), their permeability increases, enhancing the molecular exchange between the cell and its environment. This phenomenon, known as electroporation or electroporabilization, enables processes like gene transfection [1,2] and chemotherapy [3,4] to be performed much more efficiently. Molecular dynamics simulations have suggested that the formation of pores in the lipid bilayer occurs when water molecules

align at the water-bilayer interface and are driven through the hydrophobic bilayer core by local electric field gradients [5–8]. When water molecules cross the membrane, the surrounding lipid head groups usually follow the penetrating water molecules into the pore to energetically stabilize the pore structure [6,9,10]. This restructuring of the lipid bilayer has been hypothesized to alleviate the electrotonic caused by collection of oppositely-charged ions on each side of the membrane [11,12]. As long as the electric field is sustained, the pore can further expand in size facilitating the transport of ionic/molecular species across the pore [13–15]. Nevertheless, other mechanisms have been proposed to explain the increased cell membrane permeability caused by electric pulses, such as lipid peroxidation and restructuring of the membrane due to changes in membrane protein conformation [16,17].

Electroporation has been used clinically to either directly ablate tumor tissue or transiently increase membrane permeability to enhance drug delivery at the target sites inside the cell interior. In irreversible electroporation (IRE), the cellular membrane is disrupted to generate an irrecoverable homeostatic imbalance [18–21]. In gene electrotransfer (GET) [22,23] or electrochemotherapy (ECT) [24–26], electroporation enables therapeutic molecules to be more efficiently delivered into cells. During an ECT procedure, a drug such as cisplatin [27,28] or bleomycin [29–31] is first injected into a tumor site and is shortly followed by a PEF treatment, enabling the chemotherapeutic drugs

* Corresponding author.

E-mail addresses: sweeneyd@vt.edu (D.C. Sweeney), matej.rebersek@fe.uni-lj.si (M. Reberšek), janja.dermol@fe.uni-lj.si (J. Dermol), lea.rems@fe.uni-lj.si (L. Rems), damijan.miklavcic@fe.uni-lj.si (D. Miklavčič), davalos@vt.edu (R.V. Davalos).

¹ Present address: Department of Chemical Engineering, Delft University of Technology, 2629 HZ Delft, Netherlands.

to be administered with greater potency by overcoming the cell membrane's transport barrier. Because ECT is delivered locally to the tumor site, minimal systemic side-effects present as a direct result of the treatment while retaining an equivalent or greater clinical efficacy compared to traditional chemotherapy [32–35]. GET is a non-viral gene transfer method that depends on PEF treatment to enhance the delivery of therapeutic genetic material [36,37]. By inserting DNA carrying specific genetic code into cells, GET enables targeted introduction, replacement, or inactivation of selected genes. PEF treatment has dramatically improved gene-transfer efficiencies in tissues such as liver, skin, and skeletal muscle [22,38–40].

IRE technology has been used to treat tumors in canine brain tissue [41], human and porcine liver tissue [42–45], and human and porcine pancreatic tissue [46–48]. By destroying malignant cells while mitigating damage to critical stromal tissue components [49,50], it enables the treatment of tissues around critical structures that would otherwise render the site untreatable. A notable recent improvement in IRE has been termed high-frequency IRE (HF-IRE) and replaces the long monopolar pulsing schemes traditionally used in IRE ($80 \times 100 \mu\text{s}$ -long pulses delivered at 1 Hz) with bursts of short bipolar pulses [20]. These bursts of short pulses partially mitigate intra-operative impedance changes [51] and virtually eliminate muscle contractions [20,52–54] during the treatment to potentially improve both current treatment planning algorithms [20,55] and the procedural safety for the patient due to the reduced need for neuroparalytic drugs typically required to inhibit muscle contraction. For the same reason, bursts of short pulses could also be advantageous in ECT and GET, which have historically utilized pulse widths of hundreds of microseconds to milliseconds to permeabilize the cell membrane.

In the food processing industry, however, PEFs comprised of trains of pulses of 1–10 μs are routinely used to kill pathogenic and spoilage microorganisms around vegetal and animal tissue [56,57]. Only recently has such electroporation been studied in mammalian tissue for medical applications that utilize controlled, square electrical pulses on the order of one microsecond [19,58]. The observations about PEFs with microsecond pulse widths from the field of PEF-based food processing do not directly provide information on the efficiency of these pulses to enhance molecular transport across mammalian cell membranes. Consequently, more detailed study of the molecular transport occurring between a mammalian cell and its environment is needed during these types of pulses. We thereby aimed in the present study to compare membrane permeabilization obtained with 1 μs bipolar pulses and conventional 100 μs pulses, used in IRE and ECT.

In order to characterize molecular transport induced by different pulsing protocols, we performed real-time microscopic imaging of propidium iodide (PI) transport at the single cell level during and after PEF treatment. The measured changes in PI fluorescence intensity due to the uptake and subsequent binding of PI ions to intracellular nucleic acids enabled us to calculate the time course of the effective permeability of a cell membrane. This method can be further refined and validated against mechanistic models of the electroporation and membrane permeabilization processes to advance electroporation-based treatments and therapies. The results presented herein demonstrate that high-frequency bipolar electrical pulses may be designed to achieve similar degrees of electroporation as current IRE, ECT and GET pulsing schemes, but induce more symmetrical transmembrane uptake of small molecules than conventional treatments.

2. Materials & methods

2.1. Cell preparation

Chinese hamster ovary (CHO-K1) cells were obtained from the European Collection of Authenticated Cell Cultures and grown in HAM-F12 medium (PAA, Austria) supplemented with 10% fetal bovine

serum (Sigma-Aldrich, Steinheim, Germany), 1 mM L-glutamine (StemCell Technologies, Vancouver, Canada), 5 mg/mL gentamicin (Sigma-Aldrich), and 0.01 $\mu\text{L}/\text{mL}$ penicillin-streptomycin (PAA), at 37 °C under 5% CO₂. Cells were allowed to become 70–80% confluent before being trypsinized, resuspended, and transferred into glass-bottom Lab-Tek II chambers (Nalge Nunc, Wiesbaden, Germany) (7×10^4 cells in 1 mL of growth medium) to easily observe the cells during the experiment. Cells were then incubated at 37°C under 5% CO₂ for 2 h during which they adhered to the bottom of the chamber but retained roughly spherical shape. After 2 h, the growth medium was removed and replaced with low-conductivity, isoosmotic (292 mOsm/kg) potassium phosphate electroporation buffer (KPB: 10 mM KH₂PO₄/K₂HPO₄ in a ratio of 40.5:9.5, 1 mM MgCl₂, and 250 mM sucrose; pH = 7.2; electrical conductivity of 0.16 S/m) at 25 °C containing 0.15 mg/mL propidium iodide (PI) (Life Technologies, Carlsbad, USA). As KPB is approximately 10-fold less conductive than the growth medium, it was used to reduce the electric current and minimize the effects of Joule heating on the cells during PEF treatment.

2.2. Electrode design, numerical modeling of electric field distribution, and thermal considerations

Two parallel Pt/Ir alloy (90:10) wire electrodes (0.8 mm diameter wires spaced 4 mm edge-to-edge) were inserted into the Lab-Tek II chamber seeded with cells (as described) on the bottom of the glass surface. With the goal of tightly controlling the electric field to which the cells were exposed, the electric field distribution between the electrodes was simulated numerically in COMSOL Multiphysics (Version 5.1, Comsol, Burlington, MA) using the electrostatics module. The numerical calculations showed that the cells centered between the electrodes (which were monitored in the experiments) experience practically homogeneous electric field. The electric field was simulated using a 1 V test pulse (2.2 V/cm along the midline between the electrodes) to give the normalized distribution of the electric field as a result of the applied potential (Fig. 1, center and right panels).

The energy delivered during electroporation treatment was approximated in a manner similar to [59], assuming the load may be modeled as having parallel resistive and capacitive components, $R(t)$ and $C(t)$, leading to resistive current $I_R(t)$ and capacitive current $I_C(t)$, respectively. Assuming that the resistance of the medium is constant $R(t) = R$ and ideal pulses are delivered (*i.e.* each pulse starts and ends as $V_0 = V_f = 0$), the capacitive current may be neglected, giving

$$E = \int_0^{\tau_{on}} V(t)(I_R(t) + I_C(t))dt = \int_0^{\tau_{on}} \left(\frac{V^2(t)}{R(t)} + V(t)C(t) \frac{dV}{dt} \right) dt \quad (1)$$

$$\approx \sum_{i=1}^N \frac{V_i^2}{R} \tau_i = \frac{V^2}{R} \tau_{on},$$

where $\tau_{on} = \sum \tau_i$ is the total energized time of the electrodes during the treatment scheme, N is the total number of pulses in either polarity, τ_i is the pulse width of each pulse, and V_{app} is the steady-state amplitude of the pulse. Each of the treatments was designed to have equivalent τ_{on} and the applied potentials $|V_{app}|$ in treatments B, C, and D were equivalent (500 V). Estimating the total energy delivered for treatments A, B, C, and D, $V_{hi}^2 \tau_{on}$ is considered constant and, if the resistance is also considered constant and estimated from V–I measurements as $R \approx 150 \Omega$, similar applied energies were used for each treatments B, C, and D, with treatment A having a slightly lower applied energy due to the lower potential. The estimated energy dosage delivered during treatment A is estimated to be 0.12 J and 0.33 J for treatments B, C, and D. These estimates are corroborated by the measured potentials (Fig. 2). To estimate the worst-case Joule heating experienced by the cells during treatments B, C, and D, we assume that the energy delivered to the cells

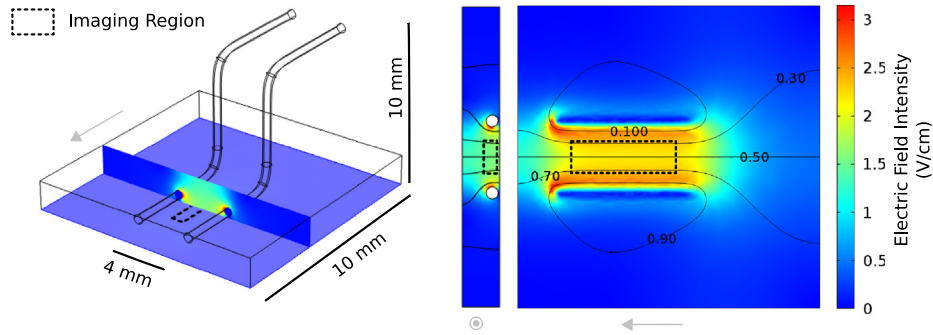


Fig. 1. Cells were exposed to electric field pulse trains using a pair of electrodes to generate a homogeneous electric field between the electrodes. From left to right: the entire electrode setup with a vertical slice showing the electric field distribution on that plane; the vertical slice from the left panel expanded; and the electric field distribution 5 μm above the bottom surface of the chamber shown in the horizontal slice in the left panel. *In vitro* application of electric fields was performed in glass-bottom chambers with Pt/Ir electrodes submerged in low-conductivity KPB pulsing medium. The electric field shown was modeled at steady state and with a voltage of 1.0 V applied to produce a relatively homogenous electric field ($\pm 3.5\%$ variation in intensity between the electrodes). The isopotential contours and the colormap indicate the distribution of the electric field within the imaging chamber and the dotted line indicates the region from which images were obtained. The gray arrows all point in the same direction to indicate the orientation of each image.

over the course of the treatment was immediately and entirely converted to heat to induce an instantaneous temperature rise as [60]

$$\Delta T = \frac{|V_{app}|^2 \sigma}{d^2 c_p \rho} \tau_{on} \quad (2)$$

where V_{app} is the amplitude of the voltage applied between the two electrodes, σ is the conductivity of the medium d is the distance separating the two electrodes, and c_p and ρ are the heat capacity and density of the medium, respectively. Assuming the properties of the medium are approximately that of water with altered conductivity ($c_p = 4200 \text{ J}/(\text{kg} \cdot \text{K})$; $\rho = 1000 \text{ kg}/\text{m}^3$; $d = 0.004 \text{ m}$; $\sigma = 0.16 \text{ S}/\text{m}$; $\tau_{on} = 0.02 \text{ s}$), we calculate that the worst-case temperature increase would be 11.9 $^\circ\text{C}$ for treatments B, C, and D. This increase would result in an increase from 25 $^\circ\text{C}$ to 37 $^\circ\text{C}$, which is approximately within the normal physiological temperature range. Furthermore, when Joule heating was considered in the finite element model of the experimental electrode configuration (results not shown), the temperature increase of the portion of the chamber in which the cells were observed was calculated to be less than 10 $^\circ\text{C}$ for treatments B, C, and D and less than 4 $^\circ\text{C}$ for treatment A.

2.3. Microscopy & fluorescent staining

Imaging was performed using an inverted fluorescence microscope (AxioVert 200, Zeiss, Oberkochen, Germany) with a 100x oil immersion objective ($NA = 1.4$). To monitor PI uptake, the cells were illuminated using a monochromator set to an excitation wavelength of 490 nm (Polychrome IV, T.I.L.L. Photonics, Munich, Germany) and the emitted PI fluorescence was detected through a 605 nm bandpass filter (605/55 nm, Chroma, Rockingham, VT) and a cooled CCD camera (VisiCam 1280, Visitron Systems, Puchheim, Germany) as described in Section 2.1 [61]. Fluorescence images (12-bit) were captured using MetaMorph 7.7.5 software (Molecular Devices, Downingtown, PA). Control images were obtained immediately prior to PEF treatment.

2.4. Time series images & pulse parameters

Time-series images were obtained by synchronizing a laboratory prototype H-bridge-based pulse generator (University of Ljubljana) with the image acquisition software using a 3 ms logical trigger pulse (5 V) from the computer controlling the image acquisition to the input trigger on the pulse generator. The triggering delay between the rising edge of the trigger pulse and the beginning of the pulsing protocol

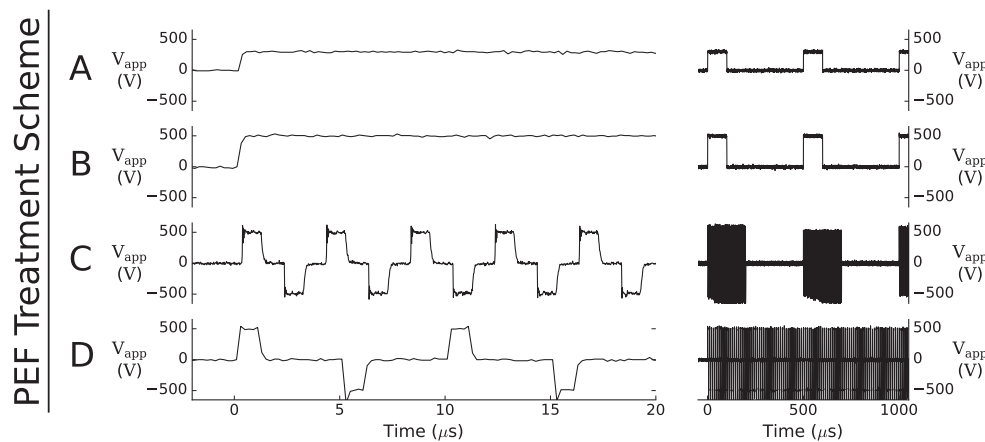


Fig. 2. Pulsed electric fields (PEFs) were applied using several schemes. Each treatment scheme is shown listed as a single row. The left plot in each row shows both voltage V_{app} trace for the first 20 μs of the applied pulse train. The right plot shows two characteristic periods of each pulsing scheme. Each treatment was performed as follows: A.) 200 monopolar pulses of 100 μs in length and 300 V amplitude; B.) 200 monopolar pulses of 100 μs in length and 500 V amplitude; C.) 200 bursts containing 50 pulses each (1×10^4 total pulses) of alternating polarity at 500 V absolute amplitude with 1 μs delay between each pulse; D.) 200 bursts containing 50 pulses each (1×10^4 total pulses) of alternating polarity at 500 V absolute amplitude with 4 μs delay between each pulse to create a continuous pulse train across the whole treatment duration. 200 periods of length 500 μs comprised each treatment scheme to conserve equivalent total treatment time across all treatments (100 ms).

was 200 ns. Pulses were applied as described above and imaging was performed at a rate of 5 Hz with the first frame being synchronized with the beginning of the pulse treatment. Oscilloscope recordings (Wavepro 7300A, LeCroy, USA) of the applied voltage V_{app} using a high voltage probe (ADP305, LeCroy) from each treatment are shown in Fig. 2. Specifically, treatment A is a train of 200 positive-polarity pulses of 300 V amplitude, each lasting 100 μ s and repeated at a rate of 2 kHz (repetition period of 500 μ s). Treatment B is exactly the same as treatment A, except with a pulse amplitude of 500 V. Treatment C is composed of 200 \times 500 μ s periods containing 50 alternating positive and negative pulses of 1 μ s duration and 500 V, separated by a 1 μ s delay between each pulse, and the whole burst followed by a 300 μ s delay before the beginning of the next burst (20,000 total pulses). Treatment D is a series of 20,000 \times 1 μ s alternating bipolar pulses of 500 V with a delay of 4 μ s between each pulse. Each treatment consisted of 200 periods ($N = 200$) lasting 500 μ s each ($T = 500 \mu$ s), for a total treatment time of exactly 100 ms for each pulsing scheme ($N \times T = 100$ ms).

2.5. Determination of cell electroporation threshold

Measurements were obtained from images captured three minutes post-treatment from cells treated with PEFs composed of waveforms similar to those appearing in treatments A & B, C, and D with varying amplitudes from 0 to 500 V, corresponding to electric field intensities of 0–1250 V/cm ($\pm 3.5\%$, depending on cells' precise location between the two electrodes). Cells were stained with PI in the same manner as described previously. To generate the electroporation threshold curves in Fig. 3, the ratio of cells containing detectable levels of PI to total cells was calculated and plotted.

2.6. Image processing

Image processing was performed using ImageJ (2.0.0) (U. S. National Institutes of Health, Bethesda, MD) and Python 3.5.1. For the time series data, images were thresholded by intensity at 0.5% of the total dynamic range of the 12-bit camera used. Within each image, a rectangular region of interest was identified around the fluorescent polar regions of the cell and the arc lengths. The corresponding arc angles within these

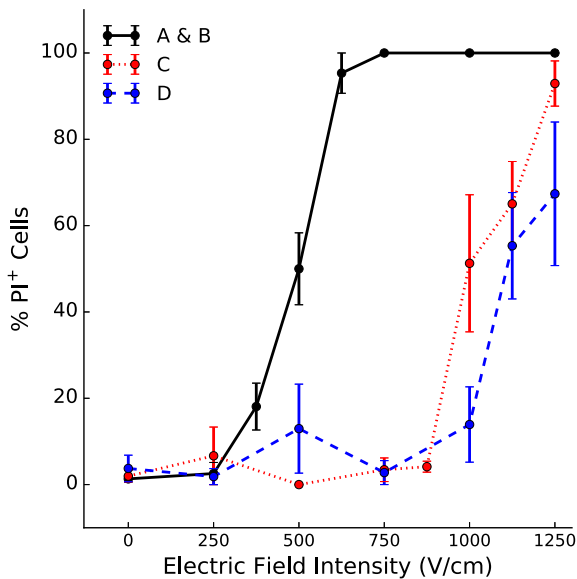


Fig. 3. Cells exposed to PEF treatments of high-frequency bipolar pulses become electroporated similarly to cells exposed to longer monopolar pulses, though at higher electric field intensities. Fluorescent images were thresholded at 1% of the camera's dynamic range and overlaid on corresponding bright field images prior to counting. If a cell contained any fluorescence above the threshold value, it was considered electroporated.

regions were calculated using additional information from bright field images taken prior to electroporation to estimate the radii of the spheroidal cells (Fig. 4). The fluorescence intensity at the anodic and cathodic poles along the cell membrane were determined by averaging 10 pixels along the radial direction for each pixel around the cell membrane to estimate the circumferential fluorescence intensity profile. The fluorescence intensity at the cell poles is reported as the average intensity of the circumferential between $\pm 5^\circ$ of the pole (90° for the anode and 270° for the cathode) normalized to the background. To quantify the anodic-cathodic crescent asymmetry, two-sample z-tests were performed for each treatment group for the anodic and cathodic electroporated arc lengths and average fluorescence intensities.

2.7. Propidium uptake calculation

The Nernst-Planck equation describes the conservation of mass in an electro-diffusion system, and has historically been used to model the mass transport in electroporated cells [62–64]. In the case of a cell in a media-filled well, the fluid is stationary. Additionally, over the time-scales observed, the image exposure time was 2 times greater than the total duration of the electrical pulses, which only took place during the first imaging frame. Therefore, the applied electric field is not present in the subsequent frames and the potential-dependent term disappears. These simplifications leave the purely diffusive Fick's law $\mathbf{J} = -\mathcal{D}_c \nabla c$ as the principle equation governing the molecular transport during the post-pulsing imaging sequences where c and \mathcal{D}_c are the concentration and diffusivity of PI, respectively, and \mathbf{J} is the flux vector. Assuming that there exists an ample concentration of PI in the cell exterior such that the concentration anywhere outside the cell along the radial direction is the same,

$$J_r = \frac{V}{\mathcal{A}} \frac{\partial c}{\partial t} = -\mathcal{D}_c \frac{\partial c}{\partial r} \quad (3)$$

where \mathcal{A} is the surface area of the cell membrane and V is the volume of the cell. The radial derivative in Eq. (3) can be discretized using $\partial c / \partial r \approx (c_{out} - c) / d_m$ and the whole equation may then be rewritten in terms of the net permeability P_m of the membrane along the outward radial direction as [62]

$$\frac{\partial c}{\partial t} = P_m (c_{out} - c), \quad (4)$$

$$P_m \approx \mathcal{D}_c \mathcal{A} / (V d_m) \quad (5)$$

where d_m is the thickness of the cell membrane. It has been shown that there exists a linear relationship between average fluorescence intensity I and concentration c of bound fluorescent PI at concentrations on the order of those in the experimental setup herein [63,65,66]. Representing this relationship as $c = \alpha I$ with proportionality constant α , and substituting this expression into Eq. (4), an expression may be found that approximates the effective membrane permeability by the equation

$$P_m = \left(\frac{1}{\alpha I_{sat} - \alpha I} \right) \frac{\partial (\alpha I)}{\partial t}, \quad (6)$$

$$= \left(\frac{1}{I_{sat} - I} \right) \frac{\partial I}{\partial t},$$

where I_{sat} is the average fluorescence intensity of the cell at saturation. Fig. 7 shows the intensity of an average cell exposed to PEF treatments A, B, C, and D. In each frame (5 Hz image acquisition rate), the average fluorescence intensity of the cell is shown on the left panel. The change in intensity over time is shown in the middle panel and indicates that the fluorescence intensity reached a maximum for cells exposed to treatment B before decaying. Using the data from treatment B to determine the saturation concentration of PI (i.e. the fluorescence intensity at $t = 10$ s) the permeability of the membrane may be determined for the

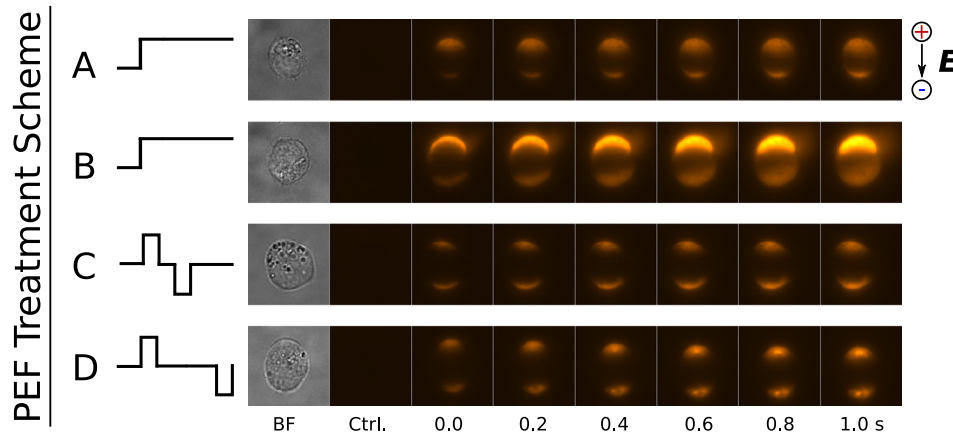


Fig. 4. Propidium fluorescence rapidly increases asymmetrically at the electropermeabilized cellular poles for long monopolar pulses and symmetrically for equivalent energy short, bipolar pulses. Images of cells are plotted every 200 ms during and post-treatment, for pulsing scheme. The anode is located at the top of each image and the cathode at the bottom, as indicated by the legend to the right of the images. Cell images are representative of typical observations for each PEF treatment scheme.

remaining treatments: A, C, and D (right panel of Fig. 7). The right panel shows the permeabilization of each cell calculated using Eq. (6). The trace for treatment B introduces a singularity in the permeabilization plot because the denominator becomes zero when the fluorescence intensity is at a maximum. This is not the case for treatments A, C, and D because they are less permeabilized and therefore are evaluated in this manner.

3. Results

3.1. Short bipolar PEFs require higher amplitudes to obtain detectable cell permeabilization compared to long monopolar PEFs

In cell populations exposed to the long, monopolar pulses in PEF treatments A and B (indicated as A & B), we detected intracellular PI at electric field intensities approximately 500 V/cm lower than in populations exposed to the bursts and continuous applications of short, bipolar pulses in PEF treatments C and D, respectively. For waveforms A & B, cell permeabilization is detected above 250 V/cm, at least 20% of the cell population is repeatably permeabilized, with the fraction of permeable cells increasing steeply until saturation at approximately 600 V/cm, where 100% of the population of cells is permeabilized as determined by measurable concentrations of PI (Fig. 3). Waveforms C and D require higher amplitude electric fields to permeabilize cells, whereby membrane permeabilization by PI can be detected above 900–1250 V/cm. However, little difference exists in the permeabilized population between C and D waveforms, with only marginally lower thresholds exhibited for the bipolar bursts in waveform C. Due to the limitations of the pulse generator, 500 V (corresponding to an electric field intensity of 1250 V/cm) was the maximum amplitude tested experimentally, which was slightly too low to achieve complete permeabilization in the case of treatments C and D.

3.2. Bipolar bursts of PEFs generate smaller, less permeabilized regions on the cell membrane than monopolar PEFs

Spatially and temporally resolved PI uptake into single cells was observed *in vitro* and quantified using images obtained during and immediately following PEF treatment (Fig. 4). The results indicate that the electropermeabilized region of the cell membrane allowing PI transport is smaller for treatments C and D than for treatments A and B. These crescent-shaped regions correspond to regions on the cell membrane that have exceeded the transmembrane potential threshold and become electropermeabilized or exhibit increased permeability. For all tested waveforms, PI uptake was detected only across membrane regions facing the anode (positive electrode) and cathode (negative electrode).

As known from previous studies, the regions of the cell membrane allowing PI transport correspond to regions of the membrane that have become destabilized and allow molecular exchange between the intracellular and extracellular environments. For monopolar waveforms A and B, the arc length of the detected permeabilized membrane region was significantly ($p < 0.0001$) larger on the anodic side compared to the cathodic side, with waveform B resulting in larger permeabilized region than treatment A (Fig. 5). Both observations are consistent with previous reports [15,17,66]. Waveform C resulted in equal arc lengths corresponding to the permeabilized membrane regions on both sides of the membrane, whereas waveform D resulted in larger arc lengths on the anodic side, but at a lower significance level ($p = 0.0454 < 0.05$), with both waveforms C and D resulting in about 50% less PI uptake at the same amplitude and treatment time as treatments B (Fig. 5). This trend is evident in Fig. 5, by the significantly lowered cathodic electropermeabilized regions in treatments C and D compared to those in treatment A and B. The much greater time rate of intensity change in Fig. 6 also indicates less surface area of the membrane is electropermeabilized and within this area, the transport of PI is reduced by 50% in treatment C, compared to treatments A and B. Significant changes in the cell's spherical shape were not apparent during the observation period with an average change in radius elicited in cells by treatment A of $-4.25 \pm 2.10\%$ ($n = 16$), by treatment B of $-6.84 \pm 1.91\%$ ($n = 15$), by treatment C of $5.62 \pm 0.61\%$ ($n = 22$), and by treatment D of $5.83 \pm 0.53\%$ ($n = 18$). The change in radius of the untreated cells was $2.27 \pm 0.93\%$ ($n = 7$; mean \pm standard error).

3.3. Membrane resealing and concentration gradients compete to limit PI influx

PI flux into an electropermeabilized cell is ultimately limited by two competing mechanisms: concentration gradients and membrane resealing (Eq. (4)). Fig. 6 shows how the fluorescence intensity time derivative along a cell's anode-to-cathode diameter (parallel to the electric field) changes over time, normalized to the cell radius. In order to become maximally fluorescent, PI must enter the cell and bind to nucleic acids. It was observed that the binding process is sufficiently rapid and occurs within microseconds of the PI entering the cell [63]. While small portions of the fluorescent region in some cells reach values near the saturation intensity of the camera sensor, the whole-cell fluorescence measurements are an average over the entire cell and plateau at a value roughly 75% of the maximum 12-bit camera sensor value (*i.e.* 4095). Therefore, the average fluorescence intensity changes within the cell are directly proportional to the PI that has entered the cell. Fig. 6 shows how the change in fluorescence intensity at the two cell poles is rapid at time $t \approx 0$, corresponding to the initial rapid entry of

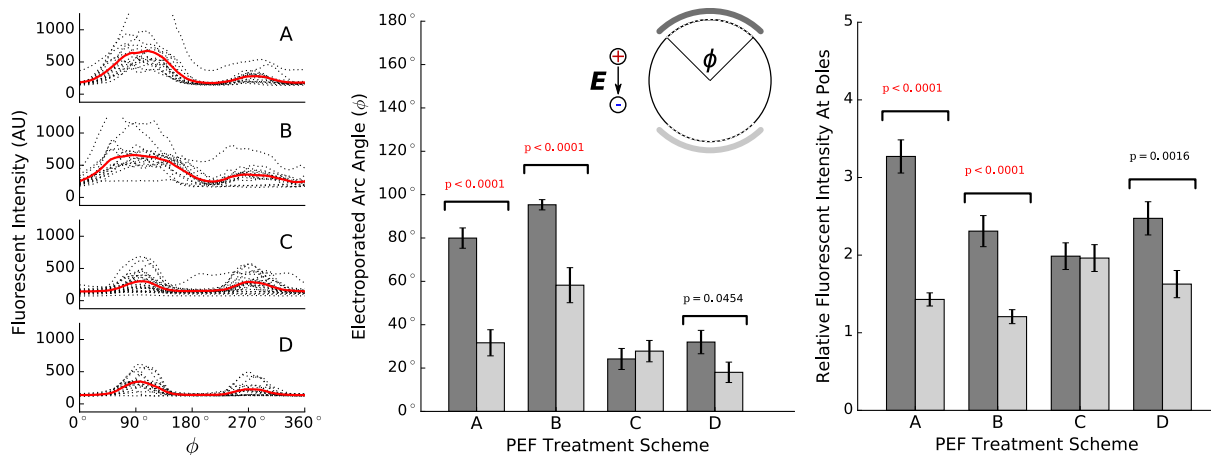


Fig. 5. The spatial extent and degree of the electroporation cap are skewed in the direction of the anode during long monopolar pulsing whereas for short bipolar pulses show more symmetric electroporated caps. Fluorescence intensity values were quantified around the circumference of each cell and plotted for each treatment (dotted black lines) and the average for each treatment group (solid red line) (left panel). Electroporated caps were identified as regions along the cell membrane exhibiting fluorescence intensity more than 0.5% of the total dynamic range of the camera with exposure of 100 ms beginning immediately following pulse treatment (middle panel). The angle ϕ is the arc angle on which 2-dimensional arc length projection lies. The fluorescence intensity average over 10° centered on the cathode and anode are shown (right panel). Statistics presented are the result of a two-sample z-test performed to compare the anodic (dark gray) and cathodic (light gray) arc lengths.

the PI into the cell unilaterally across all treatments. However, differences quickly arise when the evolution of the intensity change profile is observed between each PEF treatment. Treatments A, C, and D indicate that an initial rapid influx of PI occurs at the cell poles followed by a long, gradual decay, though the values are always positive. The asymmetries observed between the PI uptake at the cells' anodic and cathodic poles in treatment A are recapitulated in the temporal-spatial evolution profiles in Fig. 6. Following treatment B, however, the change in PI intensity reaches steady state for $t > 10$ s in treatment B, indicating that the membrane permeability has led to a relatively rapid saturation of nucleic acid binding sites. Treatments C and D of equivalent amplitude never reach this equilibrated state within the observation period (30 s post-treatment). In treatment A, the membrane never reaches the same permeabilized state as in treatment B to allow similar concentrations of intracellular PI. Because treatment B reaches equilibrium much faster than treatments A, C, and D and in each trial, the cell was exposed to the same concentration of extracellular PI, membrane permeability is the effect in treatments A, C, and D that largely limits the observed PI uptake for PEF treatments prior to reaching diffusive equilibrium.

4. Discussion

4.1. Higher amplitude is required for short bipolar PEFs to achieve similar permeabilized region sizes and degrees as longer monopolar PEFs

The degree of permeabilization and surface area of the permeabilized membrane region both depend on PEF parameters used. Here, we show that PEF treatments consisting of trains of bipolar pulses on the order of $1 \mu\text{s}$ require much greater amplitudes to generate similar levels of electroporation compared to those observed in longer pulse width monopolar PEFs (Fig. 3), for equivalent total treatment times. As determined through PI transport, these permeabilized regions appear similarly fluorescent to cells exposed to monopolar PEFs on the order of $100 \mu\text{s}$ (treatments A and B; Figs. 5). Further, in treatments A and B, (delays of $400 \mu\text{s}$ between pulses), and treatment D (delays of $4 \mu\text{s}$ between pulses), cells exhibited greater permeability on the anode-facing cell region than the cathode-facing region ($p = 0.01$). The span of the permeabilized region, in addition to the degree of permeabilization, is varied between short bipolar pulses and longer monopolar pulses and increases the net PI uptake observed *in vitro*.

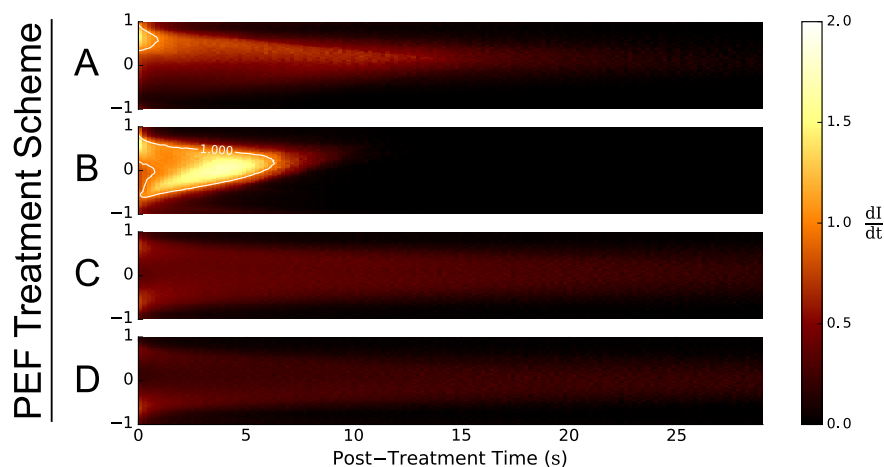


Fig. 6. Propidium flux magnitude along the normalized cellular diameter is rapid and asymmetric for long monopolar pulses while elongated and symmetric for rapid bipolar pulsing schemes. The relative change in propidium fluorescence with respect to time is calculated every $200 \mu\text{s}$ and plotted along a normalized cellular diameter where 1 and -1 correspond to the anode-facing and cathode-facing hemispheres, respectively. The time derivative is given in units of AU/s (arbitrary units per second) and where $dI/dt > 1$ is the region inside the white contour and $dI/dt < 1$ outside.

Treatment C, however induced similar degrees of permeabilization within similarly-sized regions at both poles, indicating that the mechanisms driving PI uptake occur on the time scale of $\sim 1 \mu\text{s}$.

The decreased permeabilization observed following short bipolar PEFs, despite equivalent-amplitude and equivalent treatment times, has been largely attributed to two biophysical mechanisms: incomplete charging and assisted discharge. The characteristic charging time of the cell membrane is on the order of $1 \mu\text{s}$ [68], which is two orders of magnitude smaller than the pulse width of PEFs typically used in ECT, GET, and traditional IRE. When the pulse width of the applied electric field approaches the charging time of the membrane, a significantly reduced induced transmembrane potential (Fig. 8; calculation performed as in [69], using the conductivity of the low-conductivity buffer given in Section 2.1). Low-conductivity extracellular medium typically used in *in vitro* studies to limit heating by minimizing the current flow may lengthen the membrane charging time further. If the transmembrane potential is unable to reach the same amplitude attained by short bipolar pulses as it does when longer monopolar pulses are applied, the probability of membrane permeabilization decreases.

For such short bipolar pulses, a pulse cancellation or healing mechanism has also been proposed to account for decreased PI uptake for pulses of nanosecond pulse widths (nsPEFs). While not yet rigorously explained, the second square nsPEF pulse following an initial nsPEF pulse of opposite polarity has been observed to negate a portion of the membrane restructuring induced by the first pulse [70,71]. When the delay between the first and second pulse is increased, the cancellation effect is mitigated, as if two pulses were delivered independently [72]. This cancellation mechanism could explain the greater electroporation voltage threshold (Fig. 3) in addition to the asymmetries in treatments A and B. (Fig. 5). The alternating polarity, pulse width, and intra-pulse delay on the order of the membrane charging time could account for the symmetry in electroporated region observed in treatment C: both sides of the membrane become similarly permeabilized because the differences induced on any particular side by one pulse are quickly mitigated and/or balanced by a second pulse of opposite polarity.

4.2. Propidium ions continue to enter the cell long after completion of PEF treatment

The presence of fluorescence signal indicates that the cell membrane remains permeabilized long after the conclusion of the applied electric field (Fig. 6). If electrophoresis is the dominant mechanism for propidium ion influx, the electrophoretic force acting on the propidium ions is necessarily parallel to the electric field [64,66]. The ions would enter the cell from only one of the poles, depending on their charge and the directionality of the electric field. In this case, it is possible that the electrophoretically-driven propidium ion flux would force concentrations of propidium ions into the cell membrane beyond the concentration of binding sites available. Upon removal of the electric field, intracellular diffusion would slowly allow binding of the remaining propidium ions until the binding sites are saturated with propidium ions throughout the cell, even if the membrane quickly reseals [64]. The presence of fluorescence signal in both regions following completion of monopolar PEF treatments A and B indicates that propidium ions are able to diffuse throughout the unsaturated binding sites on the cellular interior. If the permeability of the cell membrane is sufficiently large as to allow diffusive equilibration and subsequent binding-site saturation, as in the case of cells exposed to PEF treatment B, the cell's fluorescence intensity plateaus quickly and it becomes difficult to visualize changes in a cell's net permeabilization. In this case, all of the propidium ion binding sites are occupied and the fluorescence intensity will not increase further. Fig. 5 indicates that the cells exposed to treatment A (long monopolar PEFs) have larger membrane areas that

are permeabilized to a greater degree than for treatments C and D. With 60% lower amplitude, treatment A is able to generate a two-fold increase in effective permeability over treatments C and D (Fig. 3), which generate similar permeability states (Fig. 5).

Spatial observations of the regions of increased permeability *in vitro* are also important for an *in silico* model seeking to accurately describe electroporation. The electroporated membrane regions around a spherical cell must be finite for a molecule of a specific size. If a molecule is typically unable to pass through the membrane, and only through portion does transport occur, and in agreement with previous literature, the permeabilized region of the membrane is finite and dependent on the pulse parameters chosen for a given PEF treatment [62]. Though treatments A and B elicited significantly larger electroporated regions than treatments C and D (Fig. 5), the fluorescent regions of the cells in Fig. 4 are discrete and considered the only portions of the membrane to allow transmembrane transport of propidium ions [62]. The presence or absence of asymmetry in electroporated arc length has been shown to depend on the waveform of the applied electric field. For treatments comprised of long-duration monopolar pulses (100 ms), longer than those in as treatments A and B (100 μs), asymmetrical uptake of PI has been observed [66] and this effect has been replicated here with the intensity (Fig. 5) and time change of intensity on the cathodic and anodic hemispheres of the cells observed (Fig. 6).

4.3. Objective analysis of different electroporation protocols may be performed using permeability estimates

When PI binds to nucleic acids, it undergoes a dramatic fluorescence increase, making it useful in assays for evaluating membrane integrity, such as cell death [19] or membrane permeabilization [66,67], which rely on a binary result. Continuous measurements have been performed [65] using chemical agents to calibrate fluorescence intensity measurements, though they have not been used to study the temporal evolution of membrane permeability induced by electric fields with pulse widths on the order of the characteristic membrane charging time. Figs. 6 and 7 show that the fluorescence change over time has ceased and the average fluorescence intensity has plateaued at $t \approx 10 \text{ s}$, indicating that the PI binding reached a maximum. By quantifying the cell membrane's permeability, it may be possible to objectively evaluate treatments with radically different pulse parameters by comparing the effective permeability—and therefore potential molecular transport—induced by different PEF treatments. Electroporation pulse parameters of different timescales, different amplitudes, and different waveforms may be analyzed by evaluating the permeabilization they induce. Indeed, two arbitrary sets of pulse parameters may be theoretically evaluated for clinical treatment using the membrane permeabilization as an objective measurement for the efficacy of the treatment.

Complicated by the binding kinetics that generate the observed PI-based fluorescence, the ultimate fluorescence value at each point depends on the concentration distribution of nucleic acids within the cell. A valid discussion of these results is not complete without a consideration of the limits and drawbacks of this type of analysis. First, the saturation intensity I_{sat} may not correspond to an absolute concentration, but rather serves as a point of comparison between several treatment schemes. Assigning a value of I_{sat} to the maximum intensity observed allows permeability measurements to be evaluated between each treatment. Therefore, it also must be noted that the permeability measures observed are relative to a specific fluorescence value: in this case, the maximum observed in a cell. However, referenced to that point, the relative permeability induced by several different PEF treatment schemes may still be determined.

One particularly apparent drawback of calculating the relative membrane permeability in this manner is apparent in the third panel of Fig. 7: the complication that photobleaching could present. Eq. (4) indicates that the average intensity at every time point is subtracted from the average maximum intensity at saturation to resolve the calibration

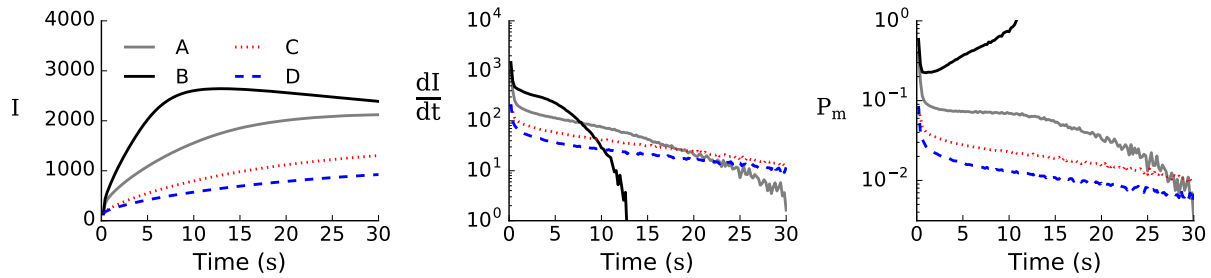


Fig. 7. The permeability induced by long, monopolar PEF treatments A and B induce significantly greater membrane permeability than short bipolar treatments C and D. The evolution of the average fluorescence intensity of the cells over time is plotted for treatments A, B, C, and D (left). The evolution of the change in fluorescence intensity over time is plotted for each of the treatments (center). Knowing the evolution of fluorescence intensity and its first derivative with respect to time enables the calculation of membrane permeability P_m using Eq. (6) (right). If, as in the case of the treatment B, the propidium concentration ceases to change while $P_m \neq 0$, as evidenced by the continued change in the other treatment plots in Fig. 6, diffusive equilibrium has been established quickly. This enables the calculation of the maximum saturation intensity I_{sat} used in Eq. (6) to calculate the permeability of the other treatments. Fluorescence intensity measurements I are given in arbitrary units and permeability P_m is given in s^{-1} . The effective permeability generated by treatment B reaches equilibrium quickly and creates the singularity in the P_m profile in the third panel, as the equilibrium fluorescent value induced by treatment B was used in the calculation of the other profiles using Eq. (6).

curve. When these measurements are close to the maximum average fluorescent value of the saturated cell, the denominator approaches zero ($I_{sat} - I \rightarrow 0$) and the calculation no longer reflects the effective permeability of the cell membrane near this singularity, such as for treatment B in the third panel of Fig. 7. In order for Eq. (4) to reflect a realistic estimate of the relative permeability of one treatment with respect to a reference, the average fluorescence intensity of the cell I must be sufficiently lower than the reference point I_{sat} .

4.4. Clinical implications for bursts of short bipolar microsecond pulsing schemes

Recently, reports of *in vivo* high-frequency IRE (HF-IRE) treatments have shown that bursts of pulses of $1 \mu s$ widths and alternating polarities (bursts similar to those in treatment C), applied at a repetition frequency of 1 Hz, could be useful in the clinical setting. These HF-IRE pulses overcome the need for pre-operative neuromuscular treatment and intra-operative cardiac synchronization when performing IRE treatments [19,20,49]. If incomplete charging is the primary mechanism driving decreased cell permeability at similar amplitudes using shorter pulse widths, the lack of muscle contractions observed in HF-IRE could be the result of a similar mechanism. By not sufficiently charging neurons to generate an action potential with a single pulse, then quickly

discharging them with an electrical pulse of opposite polarity to exploit an assisted discharge effect, a much greater probability exists that neurons may never reach the necessary voltage threshold for the necessary duration to elicit an action potential [73]. Through such a mechanism, cellular electroporation (Fig. 4) may still occur, but without the muscle contractions induced by excited nervous tissue.

In overcoming these challenges, HF-IRE has the potential to enable electroporation-based treatments with reduced pain in an out-patient clinical environment. HF-IRE, however, presents the added challenge of rendering the cell membrane significantly less permeabilized (treatments C and D) than the traditional longer monopolar pulses at similar pulse amplitudes and total treatment times (treatments A and B), as observed in Fig. 5. It should be noted that the low-conductivity buffer used in this study artificially increases the transmembrane potential rise time by limiting the electrical charge allowed to build on either side of the membrane. In so doing, the system deviates from an *in vivo* scenario with higher-conductivity extracellular media, but may still explain the increased potential threshold requirement for electroporation using HF-IRE over IRE. The results of this *in vitro* study do not exactly mirror an *in vivo* tissue, but instead serve to highlight the differences between different clinically relevant PEF treatment parameters and identify a possible mechanism to explain the differences observed on the cellular level when different pulse parameters are applied. It must be noted, however, that this study was expressly designed to study electroporation and subsequent transport immediately post-treatment. The viability of cells will decrease following exposure to temperatures in excess of $40^\circ C$ for extended periods of time [74], whereas the observational period for this study was immediately prior to, during, and post-treatment for 30 s and the temperature increase increased the temperature yet remained within a physiological range ($\Delta T \approx 12^\circ C$ from $25^\circ C$ to $37^\circ C$). Therefore long-term thermal damage (*i.e.* protein denaturation, *etc.*) affecting cellular viability was not considered in this work.

The practical implication of using HF-IRE treatments over IRE is that greater-intensity electric fields must be applied to offset the decreased transport while retaining the potential utility of HF-IRE treatments. The challenges presented by HF-IRE's shorter pulse widths may be mitigated through using higher pulse amplitudes to maximize the total membrane permeability (Fig. 3), while retaining its benefits of overcoming the need for neuromusculars and generating more homogeneous lesions. The electrical stimulation threshold required to generate action potentials in neurons increases with decreasing pulse widths [73], which allows the short bipolar electrical pulses used in HF-IRE to remain below these thresholds yet still effectively electroporate cells [20], as demonstrated here. *In silico* modeling of electroporation is particularly useful and may provide a numerical method for further optimizing pulse parameters to achieve similar effectiveness

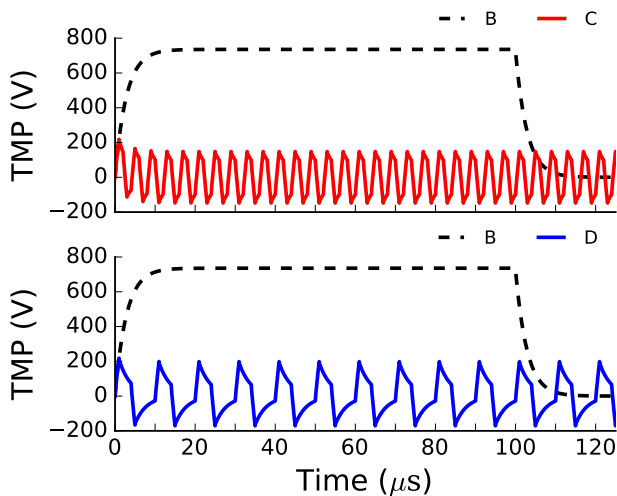


Fig. 8. The transmembrane potential TMP for short bipolar PEFs are unable to achieve the same amplitudes as longer monopolar pulses in low-conductivity medium. The calculation is based on solving the Laplace equation for electric potential in the frequency domain to determine the transient response of a cell in the presence of PEF treatments with equivalent-amplitude pulsing schemes B, C, and D with rise times of 20 ns.

as IRE while retaining the tangible *in vivo* benefits HF-IRE offers for patient care.

5. Conclusion

Clinical electrochemotherapy, gene electrotransfer, and irreversible electroporation treatments directly depend on cell membrane permeabilization and consequent transmembrane molecular transport of small molecule drugs to perturb cellular homeostasis. Real-time imaging and subsequent single-cell analysis were performed on cells exposed to pulsed electric fields composed of significantly different pulse parameters and schemes. The effective cellular membrane permeability was calculated using saturated cells to determine the maximum fluorescence intensity of PI-saturated nucleic acids. Fick's law was used to calculate the change in permeability over time for cells treated with each pulsing scheme. Cells treated with short bipolar pulses delivered in bursts of rectangular pulses on the order of 1 μ s with a 1 μ s inter-pulse delay produce more symmetric permeabilization, in both size and degree, at the extreme cathodic and anodic regions along the cell membrane while exhibiting a higher electroporation threshold. These data were observed through transport and subsequent binding of PI across the cell membrane and suggest that efficient membrane permeabilization may be achieved using high-frequency bipolar bursts of electrical pulses. The permeabilization of cells using HF-IRE may be achieved at the cost of greater electric field amplitudes to overcome the challenges presented by electric fields with pulse-widths on the order of the membrane charging time. These results indicate that HF-IRE type electrical pulses are able to generate similar, though more symmetrical permeabilization, which translates to more predictable cellular response and, therefore, may ultimately result in greater clinical precision when performing IRE, ECT, and GET procedures.

Transparency document

The Transparency document associated with this article can be found, in online version.

Acknowledgements

The authors would like to acknowledge NSF IGERT DGE-0966125 (MultiSTEPS), NIH 1R21 CA192041-01, and the USA-Slovenian Scientific Cooperation: Treatment planning for electrochemotherapy and non-thermal irreversible tissue electroporation (2014-2015) BI-US/14-15-016 funded by Slovenian Research Agency (ARRS). This work was conducted within the scope of European Associated Laboratory of Pulsed Electric Fields Applications in Biology and Medicine (LEA-EBAM) and is based upon work from COST Action TD1104 (www.electroporation.net), supported by COST (European Cooperation in Science and Technology).

References

- [1] M. Pavlin, M. Kandušer, New insights into the mechanisms of gene electrotransfer-experimental and theoretical analysis, *Sci. Rep.* 5 (2015) 9132, <http://dx.doi.org/10.1038/srep09132>.
- [2] B. Markec, E. Skvarca, T. Dolinsek, V.P. Kloboves, A. Coer, G. Sersa, M. Cemazar, Inhibitor of endocytosis impairs gene electrotransfer to mouse muscle *in vivo*, *Bioelectrochemistry* 103 (2015) 111–119, <http://dx.doi.org/10.1016/j.bioelechem.2014.08.020>.
- [3] S. Orłowski, J. Belehradey Jr., C. Paoletti, L.M. Mir, Transient electroporation, *Biochem. Pharmacol.* 37 (24) (1988) 4727–4733, [http://dx.doi.org/10.1016/0006-2952\(88\)90344-9](http://dx.doi.org/10.1016/0006-2952(88)90344-9).
- [4] G. Sersa, J. Teissie, M. Cemazar, E. Signori, U. Kamensek, G. Marshall, D. Miklavcic, Electrochemotherapy of tumors as *in situ* vaccination boosted by immunogene electrotransfer, *Cancer Immunol. Immunother.* 64 (10) (2015) 1315–1327, <http://dx.doi.org/10.1007/s00262-015-1724-2>.
- [5] M. Tarek, Membrane electroporation: a molecular dynamics simulation, *Biophys. J.* 88 (6) (2005) 4045–4053, <http://dx.doi.org/10.1529/biophysj.104.050617>.
- [6] M.J. Ziegler, P. Thomas Vernier, Interface water dynamics and porating electric fields for phospholipid bilayers, *J. Phys. Chem. B* 112 (43) (2008) 13588–13596, <http://dx.doi.org/10.1021/jp8027726>.
- [7] L. Delemotte, M. Tarek, Molecular dynamics simulations of lipid membrane electroporation, *J. Membr. Biol.* 245 (9) (2012) 531–543, <http://dx.doi.org/10.1007/s00232-012-9434-6>.
- [8] P.T. Vernier, Z.A. Levine, M.A. Gundersen, Water bridges in electroporation bilayers, *Proc. IEEE* 101 (2) (2013) 494–504, <http://dx.doi.org/10.1109/JPROC.2012.2222011>.
- [9] I. Abidor, V. Arakelyan, L. Chernomordik, Y. Chizmadzhev, V. Pastushenko, M. Tarasevich, 246 - Electric breakdown of bilayer lipid membranes I. The main experimental facts and their qualitative discussion, *Bioelectrochem. Bioenerg.* 6 (1) (1979) 37–52, [http://dx.doi.org/10.1016/0302-4598\(79\)85005-9](http://dx.doi.org/10.1016/0302-4598(79)85005-9).
- [10] T.J. Lewis, A model for bilayer membrane electroporation based on resultant electro-mechanical stress, *IEEE Trans. Dielectr. Electr. Insul.* 10 (5) (2003) 769–777, <http://dx.doi.org/10.1109/TDEL.2003.1237326>.
- [11] C. Bae, P.J. Butler, Finite element analysis of microelectrotonic of cell membranes, *Bioelectrochem. Model. Mechanobiol.* 7 (5) (2008) 379–386, <http://dx.doi.org/10.1007/s10237-007-0093-y.Finite>.
- [12] L.C. McConnell, M.J. Miksis, P.M. Vlahovska, Continuum modeling of the electric-field-induced tension in deforming lipid vesicles, *J. Chem. Phys.* 143 (24) (2015) 243132, <http://dx.doi.org/10.1063/1.4935826>.
- [13] J.C. Weaver, Y. Chizmadzhev, Theory of electroporation: a review, *Bioelectrochem. Bioenerg.* 41 (2) (1996) 135–160, [http://dx.doi.org/10.1016/S0302-4598\(96\)05062-3](http://dx.doi.org/10.1016/S0302-4598(96)05062-3).
- [14] R.W. Glaser, S.L. Leikin, L.V. Chernomordik, V.F. Pastushenko, A.I. Sokirko, Reversible electrical breakdown of lipid bilayers: formation and evolution of pores, *Biochim. Biophys. Acta* 940 (1988) 275–287.
- [15] J. Neu, W. Krassowska, Asymptotic model of electroporation, *Phys. Rev. E* 59 (3) (1999) 3471–3482, <http://dx.doi.org/10.1103/PhysRevE.59.3471>.
- [16] M. Leguèbe, A. Silve, L.M. Mir, C. Poinard, Conducting and permeable states of cell membrane submitted to high voltage pulses: mathematical and numerical studies validated by the experiments, *J. Theor. Biol.* 360 (2014) 83–94, <http://dx.doi.org/10.1016/j.jtbi.2014.06.027>.
- [17] J. Teissie, M. Golzio, M. Rols, Mechanisms of cell membrane electroporation: a mini review of our present (lack of ?) knowledge, *Biochim. Biophys. Acta Gen. Subj.* 1724 (3) (2005) 270–280, <http://dx.doi.org/10.1016/j.bbagen.2005.05.006>.
- [18] R.V. Davalos, L.M. Mir, B. Rubinsky, Tissue ablation with irreversible electroporation, *Ann. Biomed. Eng.* 33 (2) (2005) 223–231, <http://dx.doi.org/10.1007/s10439-005-8981-8>.
- [19] M.B. Sano, C.B. Arena, K.R. Bittleman, M.R. DeWitt, H.J. Cho, C.S. Szot, D. Saur, J.M. Cissell, J. Robertson, Y.W. Lee, R.V. Davalos, Bursts of bipolar microsecond pulses inhibit tumor growth, *Sci. Rep.* 5 (2015) 14999, <http://dx.doi.org/10.1038/srep14999>.
- [20] C.B. Arena, M.B. Sano, J.H. Rossmesli, J.L. Caldwell, P.A. Garcia, M.N. Rylander, R.V. Davalos, High-frequency irreversible electroporation (H-FIRE) for non-thermal ablation without muscle contraction, *BME Online* 10 (1) (2011) 102, <http://dx.doi.org/10.1186/1475-925X-10-102>.
- [21] R.E. Neal, R. Singh, H.C. Hatcher, N.D. Kock, S.V. Torti, R.V. Davalos, Treatment of breast cancer through the application of irreversible electroporation using a novel minimally invasive single needle electrode, *Breast Cancer Res. Treat.* 123 (1) (2010) 295–301, <http://dx.doi.org/10.1007/s10549-010-0803-5>.
- [22] R. Heller, M. Jaroszeski, A. Atkin, D. Moradpour, R. Gilbert, J. Wands, C. Nicolau, *In vivo* gene electroinjection and expression in rat liver, *FEBS Lett.* 389 (3) (1996) 225–228, [http://dx.doi.org/10.1016/0014-5793\(96\)00590-X](http://dx.doi.org/10.1016/0014-5793(96)00590-X).
- [23] A.I. Daud, R.C. DeConti, S. Andrews, P. Urbas, A.I. Riker, V.K. Sondak, P.N. Munster, D.M. Sullivan, K.E. Ugen, J.L. Messina, R. Heller, Phase I trial of interleukin-12 plasmid electroporation in patients with metastatic melanoma, *J. Clin. Oncol.* 26 (36) (2008) 5896–5903, <http://dx.doi.org/10.1200/JCO.2007.15.6794>.
- [24] B. Mali, T. Jarm, M. Snoj, G. Sersa, D. Miklavcic, Antitumor effectiveness of electrochemotherapy: a systematic review and meta-analysis, *Eur. J. Surg. Oncol.* 39 (1) (2013) 4–16, <http://dx.doi.org/10.1016/j.ejso.2012.08.016> (arXiv:ID: DARE-12013002662).
- [25] D. Miklavcic, B. Mali, B. Kos, R. Heller, G. Serša, Electrochemotherapy: from the drawing board into medical practice, *Biomed. Eng. Online* 13 (1) (2014) 29, <http://dx.doi.org/10.1186/1475-925X-13-29>.
- [26] C. Cabula, L.G. Campana, G. Grilz, S. Galuppo, R. Bussone, L. De Meo, A. Bonadies, P. Curatolo, M. De Laurentiis, M. Renne, S. Valpione, T. Fabrizio, N. Solari, M. Guida, A. Santoriello, M. D'Aiuto, R. Agresti, Electrochemotherapy in the treatment of cutaneous metastases from breast cancer: a multicenter cohort analysis, *Ann. Surg. Oncol.* (2015) 442–450, <http://dx.doi.org/10.1245/s10434-015-4779-6>.
- [27] G. Sersa, M. Cemazar, D. Miklavcic, Antitumor effectiveness of electrochemotherapy with cis-diamminedichloroplatinum(II) in mice, *Cancer Res.* 55 (15) (1995) 3450–3455.
- [28] G. Serša, B. Štabuc, M. Čemazar, B. Jančar, D. Miklavcic, Z. Rudolf, Electrochemotherapy with cisplatin: potentiation of local cisplatin antitumor effectiveness by application of electric pulses in cancer patients, *Eur. J. Cancer* 34 (8) (1998) 1213–1218, [http://dx.doi.org/10.1016/S0959-8049\(98\)00025-2](http://dx.doi.org/10.1016/S0959-8049(98)00025-2).
- [29] L.F. Glass, N.A. Fenske, M. Jaroszeski, R. Perrott, D.T. Harvey, D.S. Reintgen, R. Heller, Bleomycin-mediated electrochemotherapy of basal cell carcinoma, *J. Am. Acad. Dermatol.* 34 (1) (1996) 82–86, [http://dx.doi.org/10.1016/S0190-9622\(96\)90838-5](http://dx.doi.org/10.1016/S0190-9622(96)90838-5).
- [30] A. Gotherf, L.M. Mir, J. Gehl, Electrochemotherapy: results of cancer treatment using enhanced delivery of bleomycin by electroporation, *Cancer Treat. Rev.* 29 (5) (2003) 371–387, [http://dx.doi.org/10.1016/S0305-7372\(03\)00073-2](http://dx.doi.org/10.1016/S0305-7372(03)00073-2).
- [31] P. Quaglini, C. Mortera, S. Osella-Abate, M. Barberis, M. Illengo, M. Rissone, P. Savoia, M.G. Bernengo, Electrochemotherapy with intravenous bleomycin in the local treatment of skin melanoma metastases, *Ann. Surg. Oncol.* 15 (8) (2008) 2215–2222, <http://dx.doi.org/10.1245/s10434-008-9976-0>.
- [32] R. Heller, M.J. Jaroszeski, L.F. Glass, J.L. Messina, D.P. Rapaport, R.C. Deconti, N.A. Fenske, R.A. Gilbert, L.M. Mir, D.S. Reintgen, Phase I/II trial for the treatment of cutaneous and subcutaneous tumors using electrochemotherapy, *Cancer* 77 (5) (1996) 964–971, [http://dx.doi.org/10.1002/\(SICI\)1097-0142\(19960301\)77:5<964::AID-CNCR24-3.0.CO;2-O](http://dx.doi.org/10.1002/(SICI)1097-0142(19960301)77:5<964::AID-CNCR24-3.0.CO;2-O).
- [33] L.M. Mir, L.F. Glass, G. Sersa, J. Teissie, C. Domenge, D. Miklavcic, M.J. Jaroszeski, S. Orłowski, D.S. Reintgen, Z. Rudolf, M. Belehradek, R. Gilbert, M.P. Rols, J. Belehradek, J.M. Bachaud, R. DeConti, B. Stabuc, M. Cemazar, P. Coninx, R. Heller,

- Effective treatment of cutaneous and subcutaneous malignant tumours by electrochemotherapy, *Br. J. Cancer* 77 (12) (1998) 2336–2342, <http://dx.doi.org/10.1038/bjc.1998.388>.
- [34] R. Heller, R. Gilbert, M.J. Jaroszeski, Clinical applications of electrochemotherapy, *Adv. Drug Deliv. Rev.* 35 (1) (1999) 119–129, [http://dx.doi.org/10.1016/S0169-409X\(98\)00067-2](http://dx.doi.org/10.1016/S0169-409X(98)00067-2).
- [35] T. Stepišnik, T. Jarm, A. Grošelj, I. Edhemović, M. Đokić, A. Ivanec, B. Trotovec, E. Breclj, S. Potrč, M. Čemažar, N. Glumac, T. Pečnik, B. Verberič, E. Gadžijev, P. Strojjan, Electrochemotherapy: an effective method for the treatment of tumors with a combination of chemotherapeutic agent and electric field, *Zdrav. Vestn.* 85 (1) (2016) 41–55.
- [36] E. Neumann, M. Schaefer-Ridder, Y. Wang, P.H. Hofschneider, Gene transfer into muscle myoma cells by electroporation in high electric fields, *EMBO J.* 1 (7) (1982) 841–845, <http://dx.doi.org/10.1385/1-59259-409-3:55>.
- [37] T.-K. Wong, E. Neumann, Electric field mediated gene transfer, *Biochem. Biophys. Res. Commun.* 107 (2) (1982) 584–587, [http://dx.doi.org/10.1016/0006-291X\(82\)91531-5](http://dx.doi.org/10.1016/0006-291X(82)91531-5).
- [38] L.M. Mir, M.F. Bureau, J. Gehl, R. Rangara, D. Rouy, J.M. Caillaud, P. Delaere, D. Branellec, B. Schwartz, D. Scherman, High-efficiency gene transfer into skeletal muscle mediated by electric pulses, *Proc. Natl. Acad. Sci. U. S. A.* 96 (8) (1999) 4262–4267, <http://dx.doi.org/10.1073/pnas.96.8.4262>.
- [39] F.M. André, J. Gehl, G. Sersa, V. Prémat, P. Hojman, J. Eriksen, M. Golzio, M. Cemazar, N. Paveselj, M.-P. Rols, D. Miklavčič, E. Neumann, J. Teissié, L.M. Mir, Efficiency of high- and low-voltage pulse combinations for gene electrotransfer in muscle, liver, tumor, and skin, *Hum. Gene Ther.* 19 (11) (2008) 1261–1271, <http://dx.doi.org/10.1089/hum.2008.060>.
- [40] A.C. Durieux, R. Bonnefoy, T. Busso, D. Freyssenet, In vivo gene electrotransfer into skeletal muscle: effects of plasmid DNA on the occurrence and extent of muscle damage, *J. Gene Med.* 6 (7) (2004) 809–816, <http://dx.doi.org/10.1002/jgm.534>.
- [41] T.L. Ellis, P.A. Garcia, J.H. Rossmel, N. Henao-Guerrero, J. Robertson, R.V. Davalos, Nonthermal irreversible electroporation for intracranial surgical applications. Laboratory investigation, *J. Neurosurg.* 114 (3) (2011) 681–688, <http://dx.doi.org/10.3171/2010.5.JNS091448>.
- [42] H.J. Scheffer, M.C. Melenhorst, A.A. van Tilborg, K. Nielsen, K.M. van Nieuwkerk, R.A. de Vries, P.M. van den Tol, M.R. Meijerink, Percutaneous Irreversible Electroporation of a Large Centrally Located Hepatocellular Adenoma in a Woman with a Pregnancy Wish, *Cardiovasc. Intervent. Radiol.* 38 (4) (2015) 1031–1035, <http://dx.doi.org/10.1007/s00270-014-1041-8>.
- [43] K.P. Charpentier, F. Wolf, L. Noble, B. Winn, M. Resnick, D.E. Dupuy, Irreversible electroporation of the liver and liver hilum in swine, *HPB* 13 (2011) 168–173, <http://dx.doi.org/10.1111/j.1477-2574.2010.00261.x>.
- [44] W. Cheung, H. Kavnoudias, S. Roberts, B. Szkandera, W. Kemp, K.R. Thomson, Irreversible electroporation for unresectable hepatocellular carcinoma: initial experience and review of safety and outcomes, *Technol. Cancer Res. Treat.* 12 (3) (2013) 233–241, <http://dx.doi.org/10.7785/tcr.2012.500317>.
- [45] E. Ben-David, L. Appelbaum, J. Sosna, I. Nissenbaum, S.N. Goldberg, Characterization of irreversible electroporation ablation in vivo porcine liver, *Am. J. Roentgenol.* 198 (1) (2012) W62–8, <http://dx.doi.org/10.2214/AJR.11.6940>.
- [46] A. José, L. Sobrevalls, A. Ivorra, C. Fillat, Irreversible electroporation shows efficacy against pancreatic carcinoma without systemic toxicity in mouse models, *Cancer Lett.* 317 (1) (2012) 16–23, <http://dx.doi.org/10.1016/j.canlet.2011.11.004>.
- [47] D. Kwon, K. McFarland, V. Velanovich, R. Martin, Borderline and locally advanced pancreatic adenocarcinoma margin accentuation with intraoperative irreversible electroporation, *Surgery* 156 (4) (2014) 910–922, <http://dx.doi.org/10.1016/j.surg.2014.06.058>.
- [48] R.C.G. Martin, D. Kwon, S. Chalikhonda, M. Sellers, E. Kotz, C. Scoggins, K.M. McMasters, K. Watkins, Treatment of 200 locally advanced (stage III) pancreatic adenocarcinoma patients with irreversible electroporation, *Ann. Surg.* 262 (3) (2015) 486–494, <http://dx.doi.org/10.1097/SLA.0000000000001441>.
- [49] C.B. Arena, M.B. Sano, M.N. Rylander, R.V. Davalos, Theoretical considerations of tissue electroporation with high-frequency bipolar pulses, *IEEE Trans. Biomed. Eng.* 58 (5) (2011) 1474–1482, <http://dx.doi.org/10.1109/TBME.2010.2102021>.
- [50] B. Kos, P. Voigt, D. Miklavčič, M. Moche, Careful treatment planning enables safe ablation of liver tumors adjacent to major blood vessels by percutaneous irreversible electroporation (IRE), *Radiol. Oncol.* 49 (3) (2015) 234–241, <http://dx.doi.org/10.1515/raon-2015-0031>.
- [51] S.P. Bhonsle, C.B. Arena, D.C. Sweeney, R.V. Davalos, Mitigation of impedance changes due to electroporation therapy using bursts of high-frequency bipolar pulses, *Biomed. Eng. Online* 14 (Suppl. 3) (2015) S3, <http://dx.doi.org/10.1186/1475-925X-14-S3-S3>.
- [52] G. Pucihar, L.M. Mir, D. Miklavčič, The effect of pulse repetition frequency on the uptake into electroporated cells in vitro with possible applications in electrochemotherapy, *Bioelectrochemistry* 57 (2002) 167–172, [http://dx.doi.org/10.1016/S1567-5394\(02\)00116-0](http://dx.doi.org/10.1016/S1567-5394(02)00116-0).
- [53] D. Miklavčič, G. Pucihar, M. Pavlovic, S. Ribarič, M. Mali, A. Maček-Lebar, M. Petkovšek, J. Nastran, S. Kranjc, M. Čemažar, G. Serša, The effect of high frequency electric pulses on muscle contractions and antitumor efficiency in vivo for a potential use in clinical electrochemotherapy, *Bioelectrochemistry* 65 (2) (2005) 121–128, <http://dx.doi.org/10.1016/j.bioelechem.2004.07.004>.
- [54] A. Županič, S. Ribarič, D. Miklavčič, Increasing the repetition frequency of electric pulse delivery reduces unpleasant sensations that occur in electrochemotherapy, *Neoplasma* 54 (3) (2007) 246–250.
- [55] M. Marcan, D. Pavliha, B. Kos, T. Forjanic, D. Miklavčič, Web-based tool for visualization of electric field distribution in deep-seated body structures and for planning electroporation-based treatments, *Biomed. Eng. Online* 14 (Suppl. 3) (2015) S4, <http://dx.doi.org/10.1186/1475-925X-14-S3-S4>.
- [56] H. Vega-Mercado, O. Martn-Belloso, B.-L. Qin, F.J. Chang, M. Marcela Góngora-Nieto, G.V. Barbosa-Cánovas, B.G. Swanson, Non-thermal food preservation: pulsed electric fields, *Trends Food Sci. Technol.* 8 (5) (1997) 151–157, [http://dx.doi.org/10.1016/S0924-2244\(97\)01016-9](http://dx.doi.org/10.1016/S0924-2244(97)01016-9).
- [57] S. Min, G.A. Evrendilek, H.Q. Zhang, Pulsed electric fields: processing system, microbial and enzyme inhibition, and shelf life extension of foods, *IEEE Trans. Plasma Sci.* 35 (1) (2007) 59–73, <http://dx.doi.org/10.1109/TPS.2006.889290>.
- [58] S.P. Bhonsle, C.B. Arena, R.V. Davalos, A feasibility study to mitigate tissue-tumor heterogeneity using high frequency bipolar electroporation pulses, *IFMBE Proc.* 37 (2012) 1140–1143, <http://dx.doi.org/10.1007/978-3-642-23508-5>.
- [59] A.M. Lebar, N.A. Kopitar, K. Ihan, G. Sersa, D. Miklavčič, Significance of treatment energy in cell electroporation, *Electro-Magnetobiol.* 17 (2) (1998) 255–262.
- [60] M. Reberšek, M. Kranjc, D. Pavliha, T. Batista-Napotnik, D. Vrtanik, S. Amon, D. Miklavčič, M. Reberšek, M. Kranjc, D. Pavliha, T. Batista-Napotnik, D. Vrtanik, S. Amon, D. Miklavčič, Blumlein configuration for high-repetition-rate pulse generation of variable duration and polarity using synchronized switch control, *IEEE Trans. Biomed. Eng.* 56 (11) (2009) 2642–2648, <http://dx.doi.org/10.1109/TBME.2009.2027422>.
- [61] T. Kotnik, G. Pucihar, D. Miklavčič, Induced transmembrane voltage and its correlation with electroporation-mediated molecular transport, *J. Membr. Biol.* 236 (1) (2010) 3–13, <http://dx.doi.org/10.1007/s00232-010-9279-9>.
- [62] M.-P. Rols, J. Teissié, Electroporation of mammalian cells: quantitative analysis of the phenomenon, *Biophys. J.* 58 (5) (1990) 1089–1098, <http://dx.doi.org/10.1371/journal.pbio.1000456>.
- [63] G. Pucihar, T. Kotnik, D. Miklavčič, J. Teissié, Kinetics of transmembrane transport of small molecules into electroporated cells, *Biophys. J.* 95 (6) (2008) 2837–2848, <http://dx.doi.org/10.1529/biophysj.108.135541>.
- [64] M. Yu, H. Lin, Quantification of Propidium Iodide Delivery with Millisecond Electric Pulses: a Model Study, 2014 1–23 (arXiv preprint arXiv:1401.6954), [arXiv:1401.6954](http://arxiv.org/abs/1401.6954).
- [65] S.M. Kennedy, Z. Ji, J.C. Hedstrom, J.H. Booske, S.C. Hagness, Quantification of electroporative uptake kinetics and electric field heterogeneity effects in cells, *Biophys. J.* 94 (12) (2008) 5018–5027, <http://dx.doi.org/10.1529/biophysj.106.103218>.
- [66] M.M. Sadiq, J. Li, J.W. Shan, D.I. Shreiber, H. Lin, Quantification of propidium iodide delivery using millisecond electric pulses: experiments, *Biochim. Biophys. Acta Biomembr.* 1828 (4) (2013) 1322–1328, <http://dx.doi.org/10.1016/j.bbmem.2013.01.002>.
- [67] M. Hibino, H. Itoh, K. Kinoshita, Time courses of cell electroporation as revealed by submicrosecond imaging of transmembrane potential, *Biophys. J.* 64 (6) (1993) 1789–1800, [http://dx.doi.org/10.1016/S0006-3495\(93\)81550-9](http://dx.doi.org/10.1016/S0006-3495(93)81550-9).
- [68] T. Kotnik, G. Pucihar, M. Reberšek, D. Miklavčič, L. Mir, Role of pulse shape in cell membrane electroporation, *Biochim. Biophys. Acta Biomembr.* 1614 (2) (2003) 193–200, [http://dx.doi.org/10.1016/S0005-2736\(03\)00173-1](http://dx.doi.org/10.1016/S0005-2736(03)00173-1).
- [69] T. Kotnik, F. Bobanović, D. Miklavčič, Sensitivity of transmembrane voltage induced by applied electric fields—A theoretical analysis, *Bioelectrochem. Bioenerg.* 43 (1997) 285–291.
- [70] A.G. Pakhomov, I. Semenov, S. Xiao, O.N. Pakhomova, B. Gregory, K.H. Schoenbach, J.C. Ullery, H.T. Beier, S.R. Rajulapati, B.L. Ibey, Cancellation of cellular responses to nanosecond electroporation by reversing the stimulus polarity, *Cell. Mol. Life Sci.* 71 (22) (2014) 4431–4441, <http://dx.doi.org/10.1007/s00018-014-1626-z>.
- [71] E.C. Gianulis, J. Lee, C. Jiang, S. Xiao, B.L. Ibey, A.G. Pakhomov, Electroporation of mammalian cells by nanosecond electric field oscillations and its inhibition by the electric field reversal, *Sci. Rep.* 5 (August 2015) 13818, <http://dx.doi.org/10.1038/srep13818>.
- [72] K.H. Schoenbach, A.G. Pakhomov, I. Semenov, S. Xiao, O.N. Pakhomova, B.L. Ibey, Ion transport into cells exposed to monopolar and bipolar nanosecond pulses, *Bioelectrochemistry* 103 (2014) 44–51, <http://dx.doi.org/10.1016/j.bioelechem.2014.08.015>.
- [73] J. Patrick Reilly, V.T. Freeman, W.D. Larkin, Sensory effects of transient electrical stimulation—evaluation with a neuroelectric model, *IEEE Trans. Biomed. Eng.* BME-32 (12) (1985) 1001–1011, <http://dx.doi.org/10.1109/TBME.1985.325509>.
- [74] J.R. Lepock, Cellular effects of hyperthermia: relevance to the minimum dose for thermal damage, *Int. J. Hypertherm.* 19 (3) (2003) 252–266, <http://dx.doi.org/10.1080/0265673031000065042>.